

Nitrogen in the amorphous-germanium network: From high dilution to the alloy phase

A. R. Zanatta and I. Chambouleyron

Instituto de Física, Universidade Estadual de Campinas, P.O. Box 6165, Campinas, São Paulo 13081, Brazil

(Received 17 December 1992; revised manuscript received 16 March 1993)

In this work experimental data referring to the structural and optoelectronic characteristics of amorphous-germanium-nitrogen thin films are presented and discussed. The nitrogen content of the *a*-Ge:N samples, deposited by the rf-sputtering technique in an Ar + N₂ atmosphere, was allowed to vary from typical impurity levels (less than 0.5 at. %) up to around 35 at. %. The material properties change depending on the nitrogen concentration, determined from a deuteron-induced nuclear reaction. The likely mechanisms of nitrogen incorporation into the solid phase are discussed, as well as the influence of the nitrogen content on the transport and optical properties of the films. A proportionality constant relating the total nitrogen concentration in the solid phase and the integrated absorption of the *in-plane* stretching vibration mode of the Ge-N dipole has been determined. It has been found that a close analogy exists between the general properties of *a*-Ge:N alloys and those measured in amorphous-silicon-nitrogen alloys.

I. INTRODUCTION

During the last 20 years the subject of amorphous semiconductors has progressed greatly so that device structures¹ such as solar cells, flat panel displays, and optical memories, are now commercially available. One major impetus of amorphous semiconductor technology is the prospect of cheap and versatile thin-film semiconductor alloys with a variable band gap over a relatively wide energy range.

The rapid progress in the device area is the result of a partial understanding of thin-film growth conditions leading to materials with much fewer structural and compositional inhomogeneities. It is well established that this is only possible when all the deposition parameters are known and mastered. However, every plasma-assisted thin-film deposition technique possesses a great, and sometimes unknown and/or uncontrollable, number of variables. System geometry and pumping performance also play a fundamental role in the final quality of the deposited material.

Amorphous-germanium-nitrogen alloys are emerging materials. Much less studied than the *a*-Si:N parent it may have interesting applications, ranging from narrow-band-gap semiconductors to insulating layers. Recent work indicates that *a*-Ge:H is an electronic material and that it may be effectively doped with nitrogen atoms.² The present results may also contribute to the understanding of variable band gap *a*-GeN:H alloys.

The optoelectronic properties of *a* semiconductors are strongly dependent on structure. The methodology used to study the structural changes produced by N alloying the *a*-Ge network has been the systematic variation of the nitrogen partial pressure in the reaction chamber while keeping constant all other deposition parameters. The procedure allows us to measure the structural changes produced by the incorporation of nitrogen in the film as a function of nitrogen content in the solid phase. Infrared (IR) spectroscopy has been used throughout the present

work. It is, perhaps, the most important available tool to determine the amount and the way by which lighter atoms bond to an amorphous network.³ Moreover, IR spectroscopy is an easy, quick, and nondestructive method.

In this work different nitrogen concentrations were included in the *a*-Ge host network. It has been found that N contents higher than ~10 at. % induce significant changes in the alloy. The pseudogap widens with nitrogen incorporation and important variations in the electronic transport are measured. The main stretching vibration modes of the Ge₃N skeletal group have been identified, as well as their strength and peak energy dependence on nitrogenation. The proportionality constant between nitrogen content and the integrated absorption of the *in-plane* asymmetric stretching mode of the Ge₃N group has been measured and found to be $K_{\text{Ge-N}} = 5 \times 10^{18} \text{ cm}^{-2}$.

II. EXPERIMENTAL

A. Sample preparation and composition

The *a*-Ge and *a*-Ge:N samples were deposited by rf sputtering a pure crystalline Ge target of 99.9995% nominal composition, in an argon (minimum purity: 99.997%) + plus nitrogen (99.999%) atmosphere. Before each deposition run the system was pumped down for several hours. The most important residual gas partial pressure corresponds to argon ($P_{\text{Ar}} \approx 5 \times 10^{-7}$ mbar), followed by nitrogen ($P_{\text{N}_2} \approx 2 \times 10^{-7}$ mbar). All other contaminants, up to an atomic mass of 80, remain with partial pressure below 10^{-7} mbar (see Table I). A growth rate of $\approx 1.3 \text{ \AA s}^{-1}$ was adopted for all the samples being reported here.

The N₂ partial pressure (P_{N_2}) in the reaction chamber was adjusted before each deposition run and kept constant during the growing process. With the exception of

TABLE I. Deposition conditions and thickness for all the samples of the present work. The background partial pressures are from a residual gas analyzer (RGA). SCCM denotes cubic centimeter per minute at STP.

Substrate temperature (°C)	Total pressure (mbar)	Deposition rate (\AA s^{-1})	Argon flow (SCCM)	rf power density (Wcm^{-2})							
220±5	1.5×10^{-2}	≈ 1.3	≈ 200	≈ 1.2							
Typical values of residual gas pressures before deposition runs											
Molecule	H ₂	He	H ₂ O	O ₂	Ar	CO ₂	(N ₂ + CO)				
P (mbar)	5×10^{-8}	4×10^{-9}	4×10^{-8}	10^{-7}	5×10^{-7}	3×10^{-8}	2×10^{-7}				
Sample thickness											
Sample No.	1	2	3	4	5	6	7	8	9	10	11
Thickness (μm)	1.15	1.04	1.00	1.13	1.00	1.03	1.04	1.08	1.04	1.02	0.65

P_{N_2} in the chamber during growth, all samples of the present work were deposited under identical conditions, having a typical thickness of around 1 μm (see Table I).

Polished intrinsic crystalline Si wafers were used as substrates for optical measurements in the 200–4000 cm^{-1} wave-number range. The absorption coefficient in the near-infrared visible (NIR-VIS) region of the spectrum was determined on films deposited, during the same deposition run, onto *Corning 7059 glass* substrates. rf sputtered chromium coplanar Ohmic contacts were used for electrical measurements.

Rutherford backscattering is used to detect high Z elements in low or medium Z matrices. Light elements in heavy Z matrices are studied by means of nuclear reactions. The nitrogen content of the present $a\text{-Ge}_3\text{N}_4$ samples was determined from a deuteron-induced nuclear reaction⁴ [$^{14}\text{N}(d,p)^{15}\text{N}$]. The method allows us to determine a nitrogen content as low as 10^{19} atoms cm^{-3} in samples having a typical thickness of 10^{-4} cm. The analysis was performed with a 4-meV van de Graaff accelerator, with an incident deuterium beam of 610 keV.

Table II shows the nitrogen concentration (cm^{-3}) of the sample series. From these concentrations the percent nitrogen content in the alloys has been determined by interpolating between pure Ge and stoichiometric $\beta\text{-Ge}_3\text{N}_4$. Use has been made of the experimental values^{5,6} of the germanium nitride density ($\rho = 5.3 \text{ g cm}^{-3}$), the $\beta\text{-Ge}_3\text{N}_4$ phenacite structure having 4.6×10^{22} nitrogen atoms cm^{-3} .

B. Optoelectronic characterization

The dark conductivity ($\approx 120\text{--}400 \text{ K}$ range) of the films was measured in an evacuated chamber, using a digital electrometer connected to a microcomputer. Besides the acquisition of electric data and the corresponding sample temperature, the microcomputer was used to control the temperature variation rate of the sample ($\approx 3 \text{ K min}^{-1}$ in the present work). The samples were vacuum annealed during ≈ 20 min at 400 K before the conductivity versus temperature measurements. The experimental conductivity data were then computer processed in order to obtain, with the help of linear regression methods, the best fit to theoretical predictions.

The optical transmission data, from a $\lambda\text{-}9$ Perkin-

Elmer spectrophotometer, were processed to obtain⁷ the film thickness (see Table I), the index of refraction, and the absorption coefficient.

The strength, the width, and the position of the absorption bands corresponding to Ge-N vibrations were obtained from IR data using curve-fitting computer programs. The transmission spectra were obtained from Fourier-transform spectrophotometers in the *mid* and *far* IR energy ranges using the Perkin-Elmer FT1600 model and the Bio-Rad FTS-40 model apparatuses, respectively.

III. RESULTS

A. Transport properties: dc dark conductivity

It has been experimentally found that the addition of nitrogen to the argon plasma during the deposition process affects the conductivity of the $a\text{-Ge}$ films in a way that depends on the relative nitrogen partial pressure (P_{N_2}).

Figure 1 shows the dependence on temperature (T) of the dc dark conductivity (σ_d) of some selected $a\text{-Ge}_3\text{N}_4$ samples. The transport data are plotted in a $\log_{10}\sigma_d$ versus $T^{-1/4}$ representation. The conductivity of an in-

TABLE II. Compositional and electrical characteristics. Notes: *na* denotes not available; *b* denotes below the detectable limit.

Sample No.	P_{N_2} (mbar)	[N] (cm^{-3})	[N] (%)	σ_{RT} ($\Omega \text{ cm}$) ⁻¹
1	$< 10^{-7}$	<i>b</i>		9×10^{-3}
2	5.0×10^{-6}	<i>na</i>		1.5×10^{-2}
3	8.6×10^{-6}	<i>na</i>		1.8×10^{-2}
4	1.5×10^{-5}	1.6×10^{20}	0.2	1.8×10^{-2}
5	4.0×10^{-5}	6.0×10^{20}	0.7	1.7×10^{-2}
6	7.0×10^{-5}	9.1×10^{20}	1.1	1.5×10^{-2}
7	2.4×10^{-4}	3.0×10^{21}	3.7	1.1×10^{-2}
8	7.5×10^{-4}	8.8×10^{21}	10.8	3.5×10^{-3}
9	2.2×10^{-3}	1.8×10^{22}	22.1	2.5×10^{-5}
10	7.5×10^{-3}	2.5×10^{22}	30.6	$< 10^{-7}$
11	1.5×10^{-2}	2.9×10^{22}	35.5	$< 10^{-9}$

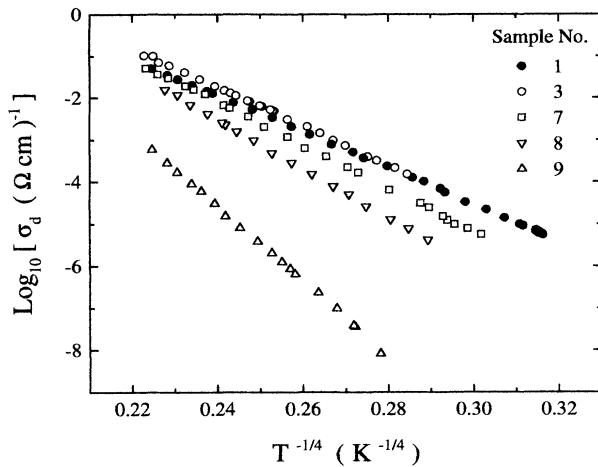


FIG. 1. Logarithm of the dark conductivity of some selected *a*-Ge:N samples vs $T^{-1/4}$. Note the straight-line fit in all cases, an indication of a variable range hopping transport mechanism.

trinsic *a*-Ge film (sample no. 1) deposited under the same conditions has also been plotted in Fig. 1. The same temperature dependence of the conductivity is measured in all the *a*-Ge:N samples of the present work below room temperature (RT).

It is well known⁸ that the electrical behavior of sputtered *a*-Ge films depends on deposition conditions and on annealing temperatures. In other words, on the density of structural defects and on thermal history. The sample series being reported here was grown under the same nominal conditions [substrate temperature, total gas pressure in the chamber, gas flow (except N_2), and rf power]. They were not annealed after deposition or prior electrical conductivity measurements. It is assumed then that the deposition conditions and the thermal history of the samples are identical and, as a consequence, the conductivity data may be compared for the purpose of electronic transport analysis.

According to Tables II and III and Fig. 1, very low P_{N_2} values ($5 \times 10^{-6} < P_{N_2} < 1.5 \times 10^{-5}$ mbar) in the reaction chamber provoke a very small increase of the

TABLE III. Optical characteristics. Notes: *na* denotes not available; *b* denotes below the detectable limit.

Sample No.	[N] (cm^{-3})	E_g (Tauc) (eV)	E_{04} (eV)	\sqrt{B} ($\text{eV cm})^{-1/2}$
1	<i>b</i>	0.71	0.84	536
2	<i>na</i>	0.70	0.86	516
3	<i>na</i>	0.71	0.85	518
4	1.6×10^{20}	0.70	0.84	518
5	6.0×10^{20}	0.70	0.86	518
6	9.1×10^{20}	0.71	0.83	513
7	3.0×10^{21}	0.69	0.84	507
8	8.8×10^{21}	0.77	0.90	450
9	1.8×10^{22}	0.95	1.16	406
10	2.5×10^{22}	2.04	2.25	340
11	2.9×10^{22}	2.11	2.48	330

room-temperature dark conductivity (σ_{RT}) and a small, but measurable, parallel upward shift of the whole conductivity curve. Increasing values of P_{N_2} , above 1.5×10^{-5} mbar, lead to a change of the slope of the $\log_{10}\sigma_d$ vs $T^{-1/4}$ curve and a conductivity decrease. The experimental data can be well fitted in all cases by Mott's $T^{-1/4}$ law,⁹

$$\sigma(T) = \sigma_0 \exp[-(T_0/T)^{1/4}], \quad (1)$$

which is indicative of a variable range hopping transport mechanism.⁹

B. Optical properties

The optical absorption of *a*-semiconductor films is usually reported in three different energy regions: (i) a *high energy region*— also called intrinsic absorption, that roughly corresponds to band-to-band transitions and where the absorption coefficient α is typically higher than 10^4 cm^{-1} ; (ii) an *intermediate energy region*— having an exponential shape normally associated with transitions involving tail states; and (iii) a *subgap absorption region*— which is associated with (a) transitions between deep defect states and the valence or conduction band, (b) local vibrations involving lighter atoms, and (c) the resonant modes of the host network.

The main results are the following.

(i) *The intrinsic absorption region.* The optical-absorption data, in the NIR-VIS energy range, were used to determine E_{04} (the photon energy corresponding to an absorption coefficient $\alpha = 10^4 \text{ cm}^{-1}$) and Tauc's optical gap E_g (defined as the energy corresponding to the extrapolated zero absorption in a $\sqrt{\alpha n E}$ versus E plot, where n is the index of refraction and E the photon energy), see Fig. 2. The slope \sqrt{B} (obtained from a $\sqrt{\alpha E}$ versus E plot) can be associated with structural disorder and corresponds to the steepness of the joint density of states of the valence- and conduction-band edges. It roughly

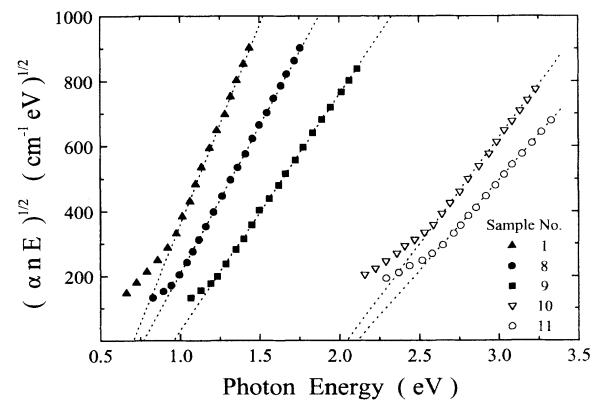


FIG. 2. Tauc's representation of the absorption edge of some *a*-Ge:N samples. The figure shows the square root of the product of the absorption coefficient (α) and the photon energy vs the photon energy. Tauc's optical gap is the energy of the extrapolated linear region (intrinsic absorption) to zero absorption.

reflects the randomness of the amorphous structure, a larger structural disorder resulting in a small \sqrt{B} .

The results of the data fitting are listed in Table III. It can be seen from the table that low nitrogen doses do not affect the optical gap (neither E_{04} nor E_g) of the host network. However, P_{N_2} in the 10^{-3} mbar range (sample nos. 8–11) widens the band gap of a -Ge, as expected.¹⁰ As in the case of a -Si:N alloys,^{11,12} an increasing N content corresponds to smaller \sqrt{B} values, a consequence of an increasing density of threefold-coordinated nitrogen atoms.¹³

(ii) *The absorption edge region.* The samples of the present work do not contain any hydrogen. As a consequence, the network contains a large density of dangling bonds producing an intense subgap absorption. Hence, the exponential absorption edge is ill defined in all the a -Ge:N samples. No relevant information could be obtained from this energy region.

(iii) *The subgap absorption region.* In the 200–4000 cm^{-1} wave-number range, vibrations of local modes associated to the presence of bonded nitrogen and resonant modes of the host a -Ge are detected. An absorption peak associated to a Ge-N stretching vibration¹⁴ appears at $\approx 690 \text{ cm}^{-1}$ in samples prepared under $P_{N_2} \geq 4 \times 10^{-5}$ mbar. Figure 3 shows the absorption coefficient versus photon wave number of the main Ge-N stretching vibration measured on sample nos. 6–11. The corresponding absorption peak of the less nitrogenated samples was below the detectable limit of the Fourier-transform infrared spectrophotometer (around ≈ 0.5 at. %). The main absorption band in Fig. 3 corresponds to the asymmetric *in-plane* Ge-N stretching vibration mode. From Fig. 3, it is clear that the absorption increases as P_{N_2} (and the nitrogen concentration [N] in the solid phase) increases. The appearance of new absorption bands is evident from the figure. The origin of these bands will be identified in the discussion section.

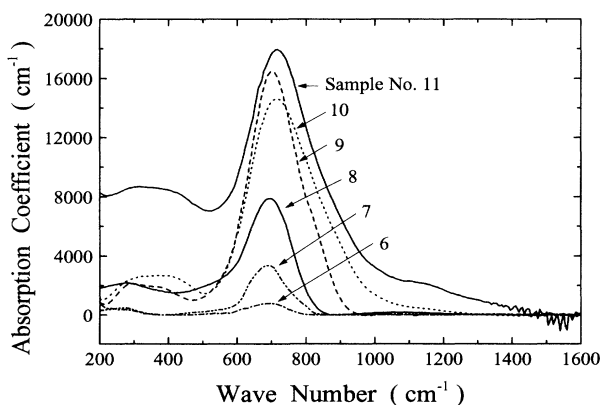


FIG. 3. Absorption coefficient vs wave number in the IR range of the a -Ge:N alloy samples. Note the appearance of new absorption bands as the nitrogen content in the films increases (see text).

IV. DISCUSSION

A. Nitrogen incorporation into the a -Ge network

The overall properties of the samples are directly related to their composition. Let us first discuss the incorporation of nitrogen into the films. Table II shows the composition of the eleven samples of the series being reported here while Fig. 4 shows the dependence of nitrogen concentration in the solid phase as a function of P_{N_2} in the chamber. Sample no. 1 has not been intentionally contaminated with nitrogen (residual $P_{N_2} \leq 2 \times 10^{-7}$ mbar) and represents the intrinsic a -Ge material. Samples labeled 2–11 were grown with increasing P_{N_2} in the chamber.

The problem of nitrogen incorporation into different materials has been addressed in the literature.^{15–17} However, the large number of different materials into which the role of nitrogenation has been studied, as well as the numerous methods used for such a purpose, prevent a unified analysis. It is known, however, that it is highly dependent on the following: (i) *gas partial pressures*, which determine the mean free path for collisions of the molecules and influences whether the reactions occur at the growing surface, in the gas, or at the target surface; (ii) *the gas flow* giving the residence time of the different species; (iii) *the substrate bias and temperature* which control the chemical reactions at the growing surface; and (iv) *the rf power fed into the plasma* which determines the ionization and dissociation rates of the gases, and the deposition rate. Other deposition parameters may affect the film properties and composition, the overall process being very complex.

It is worth mentioning at this point that varying P_{N_2} between different deposition runs while keeping a con-

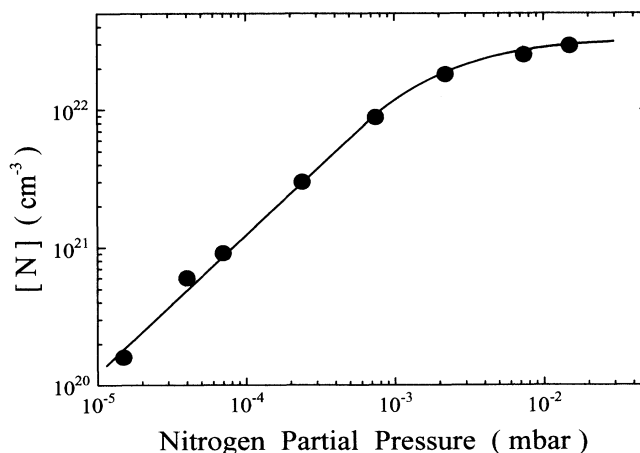


FIG. 4. Nitrogen concentration (solid phase) vs nitrogen partial pressure in the chamber during film deposition. A linear relationship exists between both parameters up to partial pressures of nearly 10^{-3} mbar. Higher N_2 partial pressures indicate a saturation process. See discussion.

stant total pressure in the chamber means that the Ar partial pressure is also varying. A simple calculation indicates that the mean free path is 15% higher in the almost pure Ar atmosphere of the less nitrogenated samples than in sample no. 11. A smaller mean free path means more frequent and less energetic collisions, decreasing both the dissociation rate of N_2 molecules and the deposition rate. This may be the origin of the saturationlike process appearing at N_2 pressures higher than $\approx 10^{-3}$ mbar (see Fig. 4). This saturation phenomenon has been observed to occur in other materials.^{15,17,18} Note that for P_{N_2} up to $\approx 10^{-3}$ mbar, the experimental data of Fig. 4 indicate a proportionality between P_{N_2} and $[N]$ in the solid phase. This is an indication that at low P_{N_2} the incorporation of nitrogen is limited by the availability of N_2 molecules in the gas phase. A decrease of the deposition rate at high P_{N_2} has been detected, a consequence of chemical reactions occurring, predominantly, at the target surface (the sputtering yield of germanium nitride is smaller than that of pure germanium).

B. Electronic transport

Mott¹⁹ calculated the electronic transport due to phonon-assisted hopping between localized states in amorphous materials [see Eq. (1)]. The prefactor σ_0 and the parameter T_0 in Eq. (1) can be expressed as

$$\sigma_0 = e^2 a^2 \nu_{ph} N(E_F) \quad (2)$$

and

$$T_0 = \lambda \gamma^3 / k_B N(E_F), \quad (3)$$

where e is the electronic charge, a is the hopping distance, ν_{ph} is a phonon frequency ($\approx 10^{13}$ s⁻¹), $N(E_F)$ is the density of localized states at the Fermi energy, γ is the inverse rate of fall off of the wave functions associated with localized states, and k_B is the Boltzmann constant. λ is a dimensionless constant ranging from 16–19.

As expected for a material having a large density of defects, a well-defined straight-line fit is obtained in a $\log_{10} \sigma_d$ vs $T^{-1/4}$ plot (see Fig. 1), which is typical of a variable range hopping conduction mechanism. The analysis of the present conductivity data gives the σ_0 and T_0 values appearing in Table IV. From them it is, in principle, possible to determine $N(E_F)$ and γ . However, as pointed out in Refs. 8 and 20, unreasonable values for $N(E_F)$ and γ may result from small deviations to the true fit. Moreover, there is some uncertainty regarding ν_{ph} . Some authors²¹ consider that this phonon frequency may be two orders of magnitude smaller than the corresponding one in the crystalline lattice. In the present case, the defect densities at the Fermi energy determined from the fit to experimental values are unreasonably low (of the order of 10^{15} cm⁻³ eV⁻¹). These are the defect densities characteristic of state-of-the-art *a*-Si:H films possessing a thermally activated dark conductivity down to low temperatures.

The localization length of the electronic wave function is inversely proportional to the square root of the binding

TABLE IV. Transport analysis. The parameters σ_0 and T_0 are those corresponding to Eqs. (1), (2), and (3). The density of states at the Fermi level was estimated using a constant γ value ($\gamma^{-1} = 10$ Å).

Sample No.	σ_0 (Ω cm) ⁻¹	T_0 (K)	$N(E_F)$ (cm ⁻³ eV ⁻¹)
1	1.6×10^8	9.0×10^7	1.7×10^{18}
2	2.7×10^8	9.1×10^7	2.3×10^{18}
3	3.3×10^8	9.1×10^7	2.4×10^{18}
4	2.2×10^8	9.6×10^7	1.6×10^{18}
5	7.9×10^8	1.1×10^8	1.7×10^{18}
6	2.9×10^{10}	1.9×10^8	1.1×10^{18}
7	3.0×10^{10}	2.0×10^8	1.2×10^{18}
8	1.0×10^{13}	5.3×10^8	
9	1.9×10^{16}	1.6×10^9	

energy of the state.⁹ For a deep state, as the one originating from a dangling bond, the localization length should be of the order of 10 Å. Transitions between localized states cease almost to occur when the distance between defects is larger than approximately ten times the localization length. Tunneling, therefore, occurs between states which are less than 100 Å apart, which means that hopping conduction at room temperature is important when the density of states at the Fermi energy is of the order of 10^{18} cm⁻³ eV⁻¹ or higher. The present conductivity data indicate that hopping is the dominant conduction mechanism, as expected for unhydrogenated samples.

More reasonable values for $N(E_F)$ in *a*-GeN samples can be calculated using the wave-function localization parameter γ as determined by Knotek *et al.*²² in *a*-Ge. Assuming $\gamma \approx 0.1$ Å⁻¹ as determined in Ref. 22 from *a*-Ge layers of different thickness, the $N(E_F)$ obtained from the calculations are more realistic. Table IV shows these calculated $N(E_F)$'s of Ge-rich alloys. The procedure, however, is applicable only in samples having a low [N] content (up to [N] ≈ 4 at. %), in which the Fermi energy is pinned by the deep defects of the *a*-Ge network (Ge dangling bonds). As the nitrogen content into the samples increases ([N] > 4 at. %), a decrease in $N(E_F)$ is expected (due to the widening mechanism of the pseudogap) associated to a stronger localization. A quantitative analysis of nitrogen-rich samples using conductivity measurements is not possible at this stage.

C. Optical properties

1. Absorption edge

Table III and Fig. 5 indicate that the pseudogap of *a*-Ge:N alloys undergoes important changes for nitrogen concentrations higher than $\sim 10^{22}$ cm⁻³, i.e., around 10 at. % where a very significant pseudogap widening is measured. Important changes are also measured in the \sqrt{B} slope of Tauc's representation. As the concentration of nitrogen increases (N being an atom of quite different size and coordination than the host network), an increasing density of defective sites is expected to appear. The

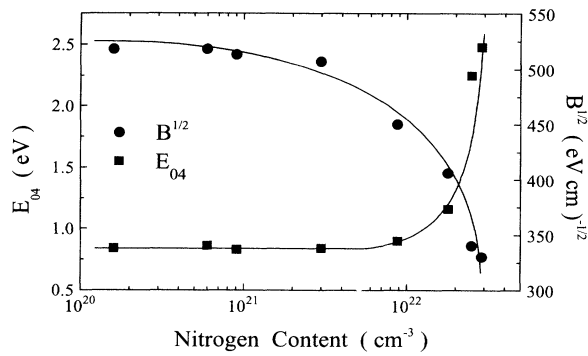


FIG. 5. Energy corresponding to an absorption coefficient of 10^4 cm^{-1} (E_{04}), and steepness of the absorption edge (\sqrt{B}) vs nitrogen content in $a\text{-Ge:N}$ samples. Note that the E_{04} energy remains constant up to a nitrogen concentration of approximately 10^{22} cm^{-3} , a higher nitrogenation producing a steep increase of the optical E_{04} gap. The effects of nitrogen on the disorder, however, are evident at smaller impurity levels (decrease of \sqrt{B}).

decreasing values of \sqrt{B} shown in Table III and Fig. 5 must be related to the erosion of the band edges (above the tails) due to a decrease of Ge-Ge bond density.¹²

The similarity of the valence structure of Si and Ge leads us to think that the gap widening mechanism in $a\text{-Ge:N}$ is similar to the one in $a\text{-Si:N}$.¹³ Structural studies of off-stoichiometric $a\text{-Ge:N}_x$ (Ref. 23) show that the local configuration or amorphous germanium nitride is similar to the one of $\beta\text{-Si}_3\text{N}_4$ with planar bonded nitrogen atoms and tetrahedral bonded silicon. This structure is consistent with sp^3 germanium hybrid orbitals while N bonding may be explained in terms of a linear combination of p orbitals, the planar geometry being given by a strong repulsion of nonbonded Ge atoms. Photoemission studies show that in $a\text{-Si:N}_x$, the valence-band maximum, dominated by Si $3p$ states in $a\text{-Si}$, recedes linearly with x . At high nitrogen concentrations the highest occupied states change over N $2p$.^{12,13} This behavior is consistent with Fig. 5 where the dependence of E_{04} on nitrogen content is shown. It is also consistent with the decrease of the film conductivity as the alloys becomes nitrogen richer (see Table II).

2. Infrared absorption: Asymmetric in-plane Ge-N mode

The group formed by a planar bonded N atom and its three germanium neighbors is the skeletal Ge_3N group. Its possible normal vibrations are the following: a breathing mode, an *out-of-plane* stretching mode, the symmetric and asymmetric *in-plane* stretching mode, and an *in-plane* bending mode. The asymmetric stretching vibration involves the displacement of the N atom and of the three Ge neighbors. It is strongly IR active and, as will be shown shortly, its strength is proportional to nitrogen concentration.

Figure 3 shows the absorption band of the asymmetric *in-plane* stretching vibration mode for the $a\text{-Ge:N}$ alloy

samples. As the nitrogen content in the material increases several effects are measured: (a) the overall absorption increases, as expected, (b) the absorption band broadens and new absorption features appear, and (c) the energy corresponding to the maximum absorption of all absorption bands shifts to higher energies.

Let us discuss these experimental findings separately.

An increased overall absorption with nitrogen content is expected simply because of an augmented density of Ge-N dipoles. The energy of the main resonance¹⁴ is centered at $\approx 690 \text{ cm}^{-1}$. The integrated absorption of the local modes has been calculated as

$$A(\omega_i) = \int [\alpha(\omega)/\omega] d\omega, \quad (4)$$

where $\alpha(\omega)$, ω , and ω_i represent the absorption coefficient, the corresponding wave number, and the peak wave number of the stretching absorption band being integrated, respectively. The asymmetric stretching *in-plane* vibration is centered at $\omega_1 \approx 690 \text{ cm}^{-1}$, but increasing nitrogen concentration in the film induces the appearance of two other satellite resonances at $\omega_2 \approx 870 \text{ cm}^{-1}$ and $\omega_3 \approx 1100 \text{ cm}^{-1}$. Their position and strength are related to new environments of the Ge-N dipoles.

Figure 6 shows the nitrogen content $[\text{N}]$, as determined from nuclear reaction data, of different $a\text{-Ge:N}$ samples versus the integrated area of (i) the main absorption band $[A(\omega_1)]$ and (ii) the whole set of stretching vibrations (ω_1 , ω_2 , and ω_3). It may be seen from the figure that the integrated absorption of the stretching bands is proportional to the nitrogen concentration in the $a\text{-Ge:N}$ films, i.e.,

$$[\text{N}] = K_{\text{Ge-N}} A(\omega_1). \quad (5)$$

The analysis of the present data indicates a proportionality constant,

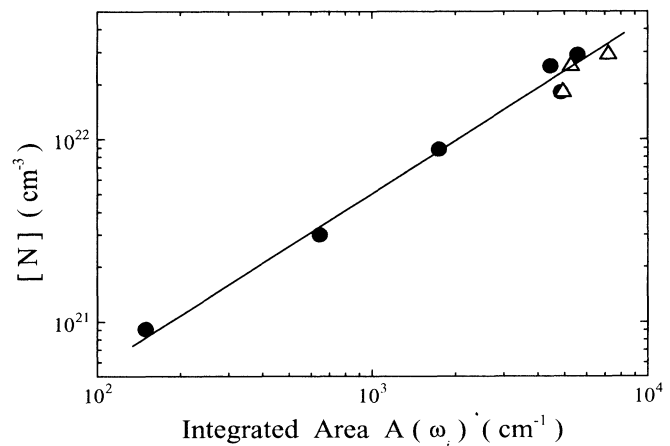


FIG. 6. Integrated absorption of the main *in-plane* stretching mode vs nitrogen content for $a\text{-Ge:N}$ samples. The slope of the straight-line fit is $K_{\text{Ge-N}} = 5.0 \times 10^{18} \text{ cm}^{-2}$. The filled circles indicate the integrated area of the absorption bands centered at about 690 cm^{-1} . The open triangles represent the integrated area of all stretching vibrations ($690, 870, \text{ and } 1100 \text{ cm}^{-1}$).

$$K_{\text{Ge-N}} = 5.0 \times 10^{18} \text{ cm}^{-2} \quad (6)$$

associated to the asymmetric *in-plane* stretching Ge-N vibration at $\omega_1 \approx 690 \text{ cm}^{-1}$.

Assuming an error of around 15 at. % in the absolute nitrogen concentration [N], associated to instrumental sensitivity limits and/or to data processing, this proportionality constant matches very well the experimental points. The errors originate mainly from uncertainties in the sample thickness, in the nuclear reaction data, and in the absolute value of the integrated absorption area. Within an overall 15 at. % error limit the experimental data indicate a perfect linear dependence of $\log_{10}[\text{N}]$ on $\log_{10}[A(\omega_1)]$ up to $[\text{N}] \approx 35$ at. %. At high nitrogen content, however, the integrated absorption data contain contributions of new satellite absorption bands which may originate some errors. Figure 6 shows that, in the present case, the integration of the whole absorption band does not modify the final result significantly.

Once a calibration constant is established by independent methods, it allows a rapid determination of alloy composition from optical measurements. The procedure has been applied to hydrogenation in *a*-Si:H and *a*-Ge:H thin films²⁴ and also to determine the nitrogen content of *a*-Si:N:H alloys.^{18,25,26} Concerning the calibration constant of nitrogen in *a*-Si:N:H alloys, however, the values given in the literature may differ by as much as one order of magnitude, going from $^{25}\text{K} = 2.9 \times 10^{18} \text{ cm}^{-2}$ to $^{26}\text{K} = 1.7 \times 10^{19} \text{ cm}^{-2}$. A likely explanation of these discrepancies may involve the use of different methods to determine the absolute concentration of nitrogen atoms. Moreover, in the case of *a*-Si:N:H films, the *in-plane* stretching vibration mode of the Si-N bonds [$\omega_1(\text{Si}) \approx 850 \text{ cm}^{-1}$] and the wagging mode of the Si-H bonds [$\omega_{\text{wag}}(\text{Si}) \approx 650 \text{ cm}^{-1}$] may overlap for high hydrogen and/or nitrogen concentrations. These sources of error are absent in the present nonhydrogenated *a*-Ge:N samples.

3. The frequency shift of the main absorption band and the appearance of satellite absorption bands

It is well established that the presence of back impurity atoms having an electronegativity different from the host network induces a shift of the peak energy of a dipole vibration.^{27,28} Depending on the electronegativity of the impurity, as related to the host atom electronegativity, the shift occurs toward lower^{29,30} or toward higher^{27-29,31,32} energies. It is worth mentioning at this point that the absence of back atom(s) [or back-atoms(s) dangling bond(s)] also influences the electronic distribution around the Ge-N dipole.³⁰

In the present alloy case the frequency shifts are associated with changes in the Ge-N interatomic distance which results from modifications in the electronic charge distribution around the germanium atom. The new charge distributions are the consequence of inductive effects produced by the back atom(s) of the dipole being considered. Nitrogen is more electronegative than germanium and, as the density of N back atom(s) increases

with nitrogenation, the degree of *s* character of the Ge-N bond increases, shortening the Ge-N bond length and increasing the effective force constant and vibration frequency. Figure 7 shows the shift of the ω_1 and ω_2 peak frequencies of the Ge_3N skeletal group as a function of E_{04} .

In the low [N] regime (sample nos. 5, 6, 7, and 8) only one absorption band is measured, centered at $\omega_1 \approx 690 \text{ cm}^{-1}$. As P_{N_2} is increased during deposition, more nitrogen atoms are incorporated into the host giving rise to inductive effects. The shift toward high frequencies is linear with N content and at $[\text{N}] \approx 10^{22} \text{ cm}^{-3}$ it amounts to 25 cm^{-1} . The measured variations are shown in Table V, where the peak position of two new absorption bands (ω_2 and ω_3) has also been indicated. The satellite bands corresponding to Ge-N dipole vibrations in different environments are detected in alloy samples having $[\text{N}] \geq 20$ at. % (see Table V).

The experimental results indicate that, in N-rich *a*-Ge:N alloys, three absorption bands associated to the asymmetric *in-plane* stretching vibration mode appear in the IR transmission spectra. The data can be well fitted by the sum of three Gaussian curves, as shown in Fig. 8. Similar IR features have been detected in *a*-SiN_x:H films having a high N concentration.³³ A possible phenomenological explanation follows (see Fig. 9).

In the relatively low nitrogen concentration range only the main absorption band at $\approx 690 \text{ cm}^{-1}$ appears. The corresponding structure is shown in Fig. 9(a) (isolated triads of Ge-N dipoles). Increasing nitrogen content in the *a*-Ge network [see Fig. 9(b)] leads to a situation where two neighboring Ge atoms are bonded to nitrogen. Inductive effects (charge redistribution around the bond) appear in both triads of Ge-N bonds producing a shift in the main vibration energy (Fig. 7). The process involves more neighboring Ge-N bonds as the nitrogen content increases and a stronger absorption is measured (Fig. 3).

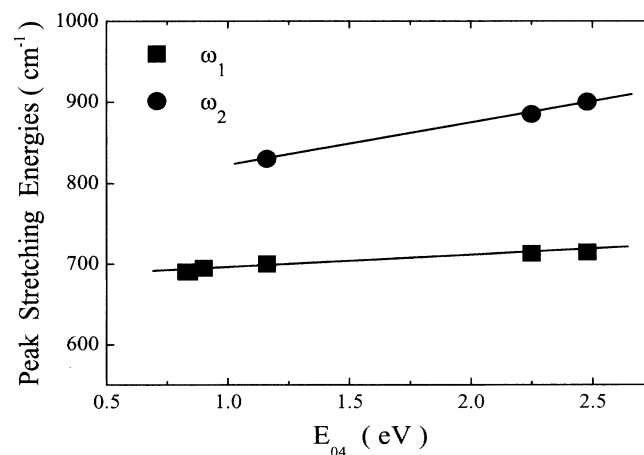


FIG. 7. Peak stretching frequencies vs the E_{04} optical gap for *a*-Ge:N alloys. Filled squares: main vibration mode. Filled circles: first satellite to the main stretching mode. The positive slope is indicative of inductive effects.

TABLE V. Absorption band characteristics. Notes: *na* denotes not available; *b* denotes below the detectable limit; $A(\omega_1)$ represents the integrated area of the absorption band of the *in-plane* stretching Ge-N vibration mode centered at ≈ 690 cm^{-1} ; ω_i indicates the peak energy of different absorption bands (see text).

Sample No.	[N] (%)	$A(\omega_1)$ (cm^{-1})	ω_1 (cm^{-1})	ω_2 (cm^{-1})	ω_3 (cm^{-1})
1					
2		<i>b</i>	<i>b</i>	<i>b</i>	<i>b</i>
3		<i>b</i>	<i>b</i>	<i>b</i>	<i>b</i>
4	0.2	<i>b</i>	<i>b</i>	<i>b</i>	<i>b</i>
5	0.7	<i>na</i>	<i>na</i>	<i>b</i>	<i>b</i>
6	1.1	150	690	<i>b</i>	<i>b</i>
7	3.7	645	690	<i>b</i>	<i>b</i>
8	10.8	1745	695	<i>b</i>	<i>b</i>
9	22.1	4840	700	830	<i>b</i>
10	30.6	4457	713	885	1120
11	35.5	5580	715	900	1130

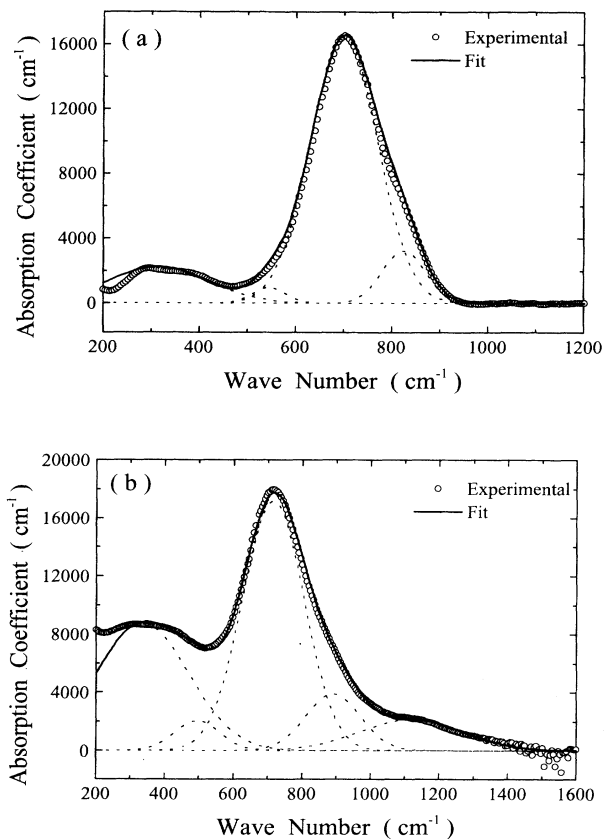


FIG. 8. Absorption spectra of *a*-Ge:N alloy films showing the several absorption bands due to nitrogenation. Note the overall increase of the integrated absorption with nitrogen content. The *disorder induced* breathing mode (≈ 300 cm^{-1}) depends on nitrogen through disorder. (a) Sample no. 9, [N]=22.1 at. %; (b) sample no. 11, [N]=35.5 at. %.

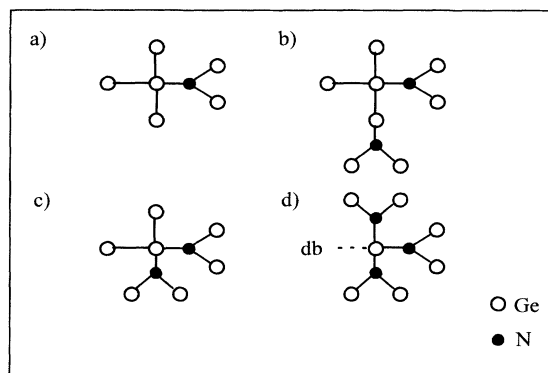


FIG. 9. Different chemical environments inducing frequency shifts of the main Ge-N dipole vibration. See text for a detailed discussion.

Possible configurations giving rise to the two new absorption bands ω_2 and ω_3 are depicted in Figs. 9(c) and 9(d), respectively. The band at 870 cm^{-1} appears when two (or more) nitrogen atoms are bonded to the same Ge atom, in a bonding configuration similar to that of the stoichiometric alloy. The absorption still corresponds to an asymmetric *in-plane* stretching Ge-N vibrational mode. At higher nitrogen concentrations, inductive effects will also shift this new vibration frequency (see Fig. 7).

The inductive effects shown in the figure indicate that, as the nitrogen concentration increases, both frequencies increase, but at a different rate. A higher slope for the more energetic vibration (ω_2) means a stronger inductive effect, giving support to the model bonding configuration shown in Fig. 9(c).

Besides an increased density of Ge-N dipoles, higher nitrogen concentrations in the alloy network are also responsible for an increased structural disorder (see the \sqrt{B} value, Table III) due either to fluctuations in the bond angles and bond lengths, or to the creation of dangling bonds. The mentioned disorder leads us to think that Ge dangling bonds induce the absorption feature detected at $\omega_3 \approx 1100$ cm^{-1} [see Fig. 9(d)]. This because the absorption features at energies higher than ≈ 890 cm^{-1} are absent in gaseous compounds (no dangling bonds) possessing Ge-N dipoles. In the solid a more energetic absorption may appear associated with a coordination defect. The above interpretation, in terms of the defective Ge_3N skeletal structure, does not rule out other possibilities.

4. Other vibration modes in the far and mid IR energy range

Crystalline Si and Ge lattices have no first-order infrared absorption. In amorphous Si and Ge, however, the lack of long-range order relaxes the crystal momentum and the symmetry rules prohibiting first-order absorption and, in principle, all vibration modes can contribute to the first-order absorption process. In other words, within a disordered network all vibration modes

can be active in the IR. In the present specific case, the introduction of nitrogen atoms into the *a*-Ge network will enhance the disorder, producing stronger IR absorption bands.^{34,35}

The disorder is at the origin of the absorption band measured at about $\approx 300\text{ cm}^{-1}$, which we identify as a *disorder induced* breathing mode, involving Ge-Ge dipole vibrations. A similar *disorder induced* Si-Si *in-plane* breathing mode, occurring at $\approx 500\text{ cm}^{-1}$, has also been detected in *a*-Si:N alloys.³⁶

The absorption band appearing at $\approx 450\text{ cm}^{-1}$ is probably associated to the symmetric *in-plane* stretching mode of the Ge_3N skeletal group. In order to proceed to a correct identification of the vibrational modes in the solid phase it is useful to compare the IR transmission spectra to the absorption features of molecules of similar symmetry. In the present case a molecule containing Ge and N atoms and having the Ge_3N structure should be studied. A compound that allows a rough analogy with the *a*-Ge:N alloy under study is trigermylamine $[(\text{GeH}_3)_3\text{N}]$, an extremely unstable and reactive gaseous species.^{37,38} The structure of the $(\text{GeH}_3)_3\text{N}$ molecule is shown in Fig. 10. The figure also contains the main vibration modes and peak positions of the gaseous species. Besides the absence of a connective network, the main difference between the samples being analyzed is the presence of hydrogen atoms as bond terminators of the three Ge atoms. Let us summarize the vibration characteristics of trigermylamine.

(i) The Ge atoms are probably *noncoplanar* in trigermylamine. A valence force field calculation³⁷ gives a bond angle of 116° at nitrogen. The vibrations of the pyramidal site for a threefold-coordinated N are qualitatively similar to the vibrations of N in a planar configuration. Both have four characteristic vibrations involving the

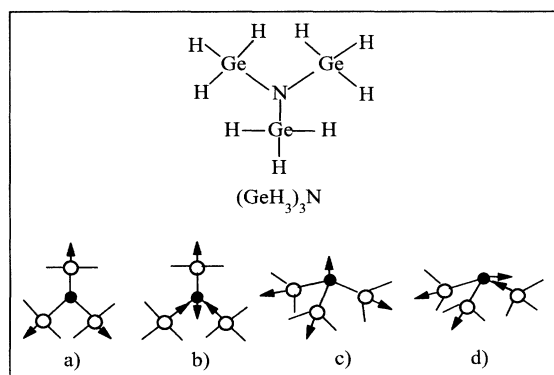


FIG. 10. Simplified skeletal representation for the trigermylamine $[(\text{GeH}_3)_3\text{N}]$ molecule (top). The possible stretching vibrations for the Ge_3N group in an *a*-Ge host (the open circles represent the Ge atoms and the dots N atoms) (Ref. 39) (a) the symmetric *in-plane* stretching vibration mode ($\approx 370\text{ cm}^{-1}$); (b) the asymmetric *in-plane* stretching vibration mode ($\approx 850\text{ cm}^{-1}$); (c) the symmetric (pyramidal configuration) stretching mode, and (d) the asymmetric near *in-plane* (pyramidal configuration) stretching mode. Vibrations (c) and (d) are characteristics of gaseous trigermylamine.

displacement of N and its three Ge neighbors.

(ii) There are two IR absorption bands in gaseous $(\text{GeH}_3)_3\text{N}$ which do not move on deuteration:^{37,38} a very strong and broad band at $\sim 850\text{ cm}^{-1}$ attributed to the asymmetric stretching mode of the Ge_3N structure, and a weak band at $\sim 370\text{ cm}^{-1}$ originating from the symmetric stretching mode of trigermylamine, respectively.

Some considerations on the vibration frequencies of the skeletal Ge_3N structure in solid *a*-Ge:N and gaseous $(\text{GeH}_3)_3\text{N}$ follow.

(a) Trigermylamine is a structure in which three hydrogen atoms are bonded to each Ge. As hydrogen is more electronegative than Ge a charge redistribution around the Ge atom is expected. As a consequence, the stretching vibrations should be more energetic in the molecule than in an isolated Ge-N dipole, as found. As the nitrogen concentration increases in *a*-Ge:N, however, the presence of N back atoms leads to a charge redistribution around the atoms going in the same direction as the one existing in trigermylamine. This fact may explain the reasonable agreement in energy of the asymmetric *in-plane* stretching vibrations in both the gaseous and the solid phases (850 and 870 cm^{-1} , respectively) of the Ge_3N skeletal group.

(b) In the present work, the absorption band at $\approx 450\text{ cm}^{-1}$ has been associated to the *in-plane* symmetric stretching mode in *a*-Ge:N. The analogous band in trigermylamine was found at 370 cm^{-1} . The energy difference may originate from the *nonplanar* configuration in $(\text{GeH}_3)_3\text{N}$ which involves the motion of the N atom.

(c) There are no Ge-Ge bonds in trigermylamine and, consequently, no absorption band at 300 cm^{-1} . The dependence of the absorption strength of the 300 cm^{-1} feature on nitrogen concentration in *a*-Ge:N lead us to think that 300 cm^{-1} vibration is a *disorder induced* Ge-Ge breathing mode.

The nature and the origin of an absorption band can be

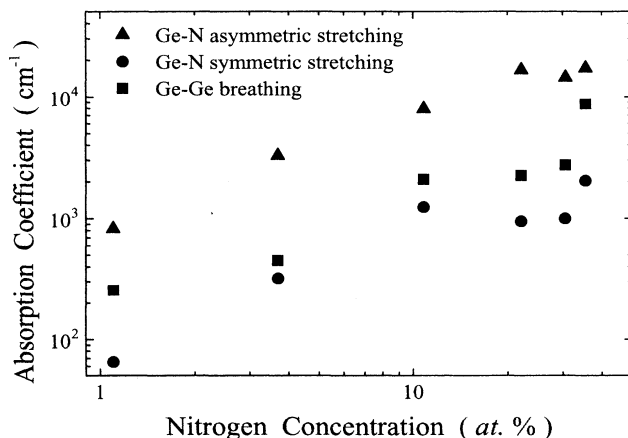


FIG. 11. Absorption coefficient at peak energy vs nitrogen concentration in the solid phase for the stretching and breathing modes of *a*-Ge:N alloys. Note the dependence on nitrogenation of all vibrational modes.

established by investigating the dependence of its strength and position on alloying. A linear relationship between absorption strength and composition with no extra bands at high alloy ratios, as well as a constant band shape, means that just the density of dipole oscillators is varying. Similarly, an equal shift of peak absorption energy with composition for two different absorption bands, or a linear relationship between maximum absorption coefficients for a couple of bands, indicate that both have a common origin.

Figure 11 shows the dependence of the absorption strength on alloying of asymmetric *in-plane* Ge-N stretching, Ge-N symmetric stretching, and Ge-Ge breathing modes at 700, 450, and 300 cm^{-1} , respectively. The overall absorption increase on alloying indicates that nitrogenation is associated with the three modes.

V. CONCLUSIONS

In this work we report a detailed study of the optoelectronic and structural characteristics of rf-sputtered amorphous-germanium-nitrogen films. The main conclusions follow.

(1) Under selected deposition conditions and system geometry two different nitrogen incorporation regimes were identified: (a) at $P_{\text{N}_2} < 10^{-3}$ mbar the nitrogen concentration in the solid phase is proportional to P_{N_2} being determined by the availability of N_2 molecules in the reaction chamber, and (b) at $P_{\text{N}_2} > 10^{-3}$ mbar the incorporation of nitrogen tends to saturate. We suggest a likely mechanism to explain this saturation phenomenon.

(2) In all samples electronic transport is dominated, below room temperature, by a variable-range-hopping-like mechanism. This behavior is consistent with a nonhydrogenated amorphous network and with measured optical properties. A calculation assuming an inverse decay constant for the localized state wave function of 0.1 \AA^{-1} (as in pure *a*-Ge) gives density of states (DOS)

at the Fermi level above $10^{18} \text{ cm}^{-3} \text{ eV}^{-1}$ in the less nitrogenated samples. Wide-band-gap *a*-Ge:N films possess a smaller DOS.

(3) The optical properties of the samples in the NIRVIS energy range exhibit a general behavior similar to *a*-Si:N films, an indication of a similar bonding configuration. Photoemission studies must be performed to give a clearer picture of the band-gap widening mechanism.

(4) The main absorption bands in the IR energy range have been identified and the dependence of their strength and shape on N content has been quantified. The absolute nitrogen content of the samples was determined from a deuteron-induced nuclear reaction [$^{14}\text{N}(d,p)^{15}\text{N}$]. A proportionality constant relating the integrated absorption of the *in-plane* stretching vibration mode and the total nitrogen content was determined: $K_{\text{Ge-N}} = 5.0 \times 10^{18} \text{ cm}^{-2}$.

(5) Inductive effects due to increasing nitrogenation have been measured in the main stretching vibration modes. The appearance of new absorption bands at ≈ 870 and $\approx 1100 \text{ cm}^{-1}$ is reported. They are tentatively ascribed to Ge-N stretching vibrations in an environment including nitrogen atoms and dangling bonds in different neighboring bonding configurations.

(6) Absorption features appearing at ≈ 450 and at $\approx 300 \text{ cm}^{-1}$ have been associated to symmetric stretching and to breathing modes involving the disordered *a*-Ge₃N and the *a*-Ge skeletal groups, respectively. Their dependence on N content was studied.

ACKNOWLEDGMENTS

This work was partially supported by the Brazilian agencies FAPESP and CNPq. The authors are indebted to Professor F. L. Freire, Jr. for the nuclear reactions analyses and to Professor P. A. Schulz and Professor C. Davanzo for fruitful discussions.

¹A. Madan and M. P. Shaw, *The Physics and Applications of Amorphous Semiconductors* (Academic, London, 1988).
²A. R. Zanatta and I. Chambouleyron, *Phys. Rev. B* **46**, 2119 (1992).
³H. Shanks, C. J. Fang, L. Ley, M. Cardona, F. G. Demond, and S. Kalbiter, *Phys. Status Solidi B* **100**, 43 (1980).
⁴M. Berti and A. V. Drigo, *Instrum. Methods* **201**, 473 (1982).
⁵G. D. Bagratishvili, R. B. Dzhanelidze, N. I. Kurdiani, and D. V. Saksaganskii, *Phys. Status Solidi A* **36**, 73 (1976).
⁶S. N. Ruddlesden and P. Popper, *Acta Crystallogr.* **11**, 465 (1958).
⁷R. Swanepoel, *J. Phys. E* **16**, 1214 (1983).
⁸D. K. Paul and S. S. Mitra, *Phys. Rev. Lett.* **31**, 1000 (1973).
⁹N. F. Mott and E. A. Davis, *Electronic Processes in Non-Crystalline Materials* (Oxford University Press, Oxford, 1971).
¹⁰I. Chambouleyron, *Appl. Phys. Lett.* **47**, 117 (1985).
¹¹F. Alvarez and I. Chambouleyron, *Sol. Energy Mater.* **10**, 151 (1984).
¹²J. Robertson, *Philos Mag. B* **63**, 47 (1991).
¹³R. Karcher, L. Ley, and R. L. Johnson, *Phys. Rev. B* **30**, 1896

(1984).
¹⁴I. Chambouleyron, F. C. Marques, J. I. Cisneros, F. Alvarez, S. Moehlecke, W. Losch, and I. Pereyra, *J. Non-Cryst. Solids* **77&78**, 1309 (1985).
¹⁵H. F. Winters and E. Kay, *J. Appl. Phys.* **43**, 794 (1972).
¹⁶C. J. Mogab, P. M. Petroff, and T. T. Sheng, *J. Electrochem. Soc.* **122**, 815 (1975).
¹⁷C. J. Mogab and M. Lugujo, *J. Appl. Phys.* **47**, 1302 (1976).
¹⁸G. Sasaki, M. Kondo, S. Fujita, and A. Sasaki, *Jpn. J. Appl. Phys.* **10**, 1394 (1982).
¹⁹N. F. Mott, *Adv. Phys.* **16**, 49 (1967).
²⁰K. P. Chik, S. Y. Feng, and S. K. Poon, *Solid State Commun.* **33**, 1019 (1980).
²¹K. P. Chik and K. C. Koon, *Philos. Mag. B* **53**, 399 (1986).
²²M. L. Knotek, M. Pollak, T. M. Donovan, and H. Kurtzman, *Phys. Rev. Lett.* **30**, 835 (1973).
²³F. Boscherini, A. Filipponi, S. Pascarelli, F. Evangelisti, S. Mobilio, F. C. Marques, and I. Chambouleyron, *Phys. Rev. B* **39**, 8364 (1989).
²⁴C. J. Fang, K. J. Gruntz, L. Ley, and M. Cardona, *J. Non-*

- Cryst. Solids **35&36**, 255 (1980).
- ²⁵A. Marimoto, Y. Tsujimura, M. Kumeda, and T. Shimizu, Jpn. J. Appl. Phys. **24**, 1394 (1985).
- ²⁶M. M. Guraya, H. Ascolani, G. Zampieri, J. I. Cisneros, J. H. D. da Silva, and M. P. Cantão, Phys. Rev. B **42**, 5677 (1990).
- ²⁷A. L. Smith and N. C. Angelotti, Spectrochem. Acta **15**, 412 (1959).
- ²⁸G. Lucovsky, Solid State Commun. **29**, 571 (1979).
- ²⁹H. Wieder, M. Cardona, and C. R. Guarnieri, Phys. Status Solidi B **92**, 99 (1979).
- ³⁰T. S. Shi, S. N. Sahu, G. S. Oehrlein, A. Hiraki, and J. W. Corbett, Phys. Status Solidi A **74**, 329 (1982).
- ³¹G. Lucovsky, in *Tetrahedrally Bonded Amorphous Semiconductors, Carefree, Arizona*, edited by R. A. Street, D. K. Biegelson, and J. C. Knights, AIP Conf. Proc. No. 73 (AIP, New York, 1981), p. 100.
- ³²G. Lucovsky, J. Phys. (Paris) Colloq. **42**, C4-741 (1981).
- ³³S. Hasegawa, H. Anbutsu, and Y. Kurata, Philos. Mag. B **59**, 365 (1989).
- ³⁴S. C. Shen, C. J. Fang, M. Cardona, and L. Genzel, Phys. Rev. B **22**, 2913 (1980).
- ³⁵M. H. Brodsky and A. Lurio, Phys. Rev. B **9**, 1646 (1974).
- ³⁶D. V. Tsu, G. Lucovsky, and M. J. Mantini, Phys. Rev. B **33**, 7069 (1986).
- ³⁷D. W. H. Rankin, J. Chem. Soc. A **1926** (1969).
- ³⁸C. Glidewell, D. W. H. Rankin, and A. G. Robiette, J. Chem. Soc. A **2935** (1970).
- ³⁹G. Lucovsky and W. B. Pollard, in *Vibrational Properties, The Physics of Hydrogenated Amorphous Silicon II*, edited by J. D. Joannopoulos and G. Lucovsky, Topics in Applied Physics Vol. 56 (Springer-Verlag, Berlin, 1984).